Spin-charge conversion in InSe bilayers

Ma Zhou,[1,2] Dong Zhang,[1,2] Shengbin Yu,[1,2] Zhihan Huang,[1,2] Yingda Chen,[1,2] Wen Yang,[3,*] and Kai Chang[1,2,†]

[1]*SKLSM, Institute of Semiconductors, Chinese Academy of Sciences, P.O. Box 912, Beijing 100083, China*
[2]*CAS Center for Excellence in Topological Quantum Computation, University of Chinese Academy of Sciences, Beijing 100190, China*
[3]*Beijing Computational Science Research Center, Beijing 100193, China*

We find that the bilayer InSe possesses an intrinsic Rashba spin-orbit coupling and hence a spin-charge conversion effect due to the breaking of mirror symmetry. The interplay between the Rashba spin-orbit coupling and the nonparabolic Mexican hat dispersion leads to an interesting intraband Lifshitz transition and strongly amplifies the spin-charge conductivity, making it larger than that in conventional two-dimensional electron gas formed at oxide interfaces. This highlights bilayer InSe as a strong candidate for next-generation spintronic devices.

I. INTRODUCTION

Layered III-VI semiconductors such as InSe and GaSe are well known for their intrinsic outstanding properties and potential applications in nonlinear optics [1–11]. Recently, their 2D counterparts also attracted much attention as the next generation of graphene-like materials. First-principles calculations [12–16] reveal an unusual nonparabolic topmost valence band (sometimes called a Mexican hat) with a large density of states (DOS) and Van Hove singularity at the top of the valence band. This leads to an interesting ferromagnetic phase transition in monolayer GaSe [16]. The recent experimental growth of few-layer GaSe and InSe [17,18] further aroused great enthusiasm for these materials [19,20]. All these few-layer III-VI semiconductors (thickness < 6) share a common feature; i.e., their topmost valence band exhibits nonparabolic, Mexican hat dispersion [18]. However, the monolayer is symmetric under the reflection about the material plane, while the AB-stacking bilayer [see Figs. 1(a) and 1(b)] breaks this mirror symmetry. Such symmetry-breaking [15] bilayer can be exfoliated from γ and ϵ InSe bulk material [21,22].

The spin-charge conversion, also known as the inverse Edelstein effect [23] or the spin-galvanic effect, is the generation of charge current from a nonequilibrium spin polarization [24]. The Rashba spin-orbit coupling (RSOC) induced by the structural inversion asymmetry is responsible for these effects taking place in quantum wells [25] and interfaces where RSOC can be tuned by gate voltage [26,27]. Recent experiments have demonstrated a large conversion efficiency for the two-dimensional electron gas formed at the interface between two insulating oxides, LaAlO$_3$ and SrTiO$_3$ [28,29]. In this work, we find an intrinsic Rashba spin-orbit coupling (IRSOC) and hence spin-charge conversion effect in bilayer InSe, based on the 20-band $\mathbf{k} \cdot \mathbf{p}$ Hamiltonian derived by

the standard invariant theory. This IRSOC arises from the breaking of the mirror symmetry combined with the atomic spin-orbit coupling. The interplay of the IRSOC and the Mexican hat dispersion near the topmost of the valence band leads to intraband Lifshitz transitions and strongly amplifies the spin-charge conductivity (S-C conductivity), making it five times higher than that in conventional oxide interface systems [29]. In addition to the $\mathbf{k} \cdot \mathbf{p}$ model, we also confirm these phenomena using the tight-binding model. The intraband Lifshitz transition and the giant S-C conductivity peak are very close ($\sim$3 meV below) to the top of the highest valence band, so observing this phenomenon only requires a small doping density (which in turn implies weak scattering and hence long carrier lifetime) and should be experimentally accessible. The two key ingredients of these effects—the RSOC and the Mexican hat dispersion—also exist in other few-layer III-VI semiconductors and strong RSOC systems, such as polarized interfaces and narrow band gap semiconductor quantum wells, so we expect this phenomenon to be universal in these systems. Since the spin-charge conversion is a central issue in spintronics [28,30–34], the enhanced S-C conductivity by our findings highlights few-layer III-VI semiconductors as strong candidates for next-generation spintronic devices [35].

The rest of this paper is organized as follows. In Sec. II, we adopt the standard invariant theory to derive the 20-band $\mathbf{k} \cdot \mathbf{p}$ Hamiltonian for the InSe bilayer. In Sec. III A, we calculate the spin-charge conversion of the InSe bilayer based on our $\mathbf{k} \cdot \mathbf{p}$ model and tight binding under the clean-limit condition. In Sec. III B, we perform further calculations to take into account the disorder effect. The summary and final conclusions are in Sec. IV.

II. TWENTY-BAND k · p HAMILTONIAN OF BILAYER METAL CHALCOGENIDE

As shown in Fig. 1, the unit cell of the bilayer InSe consists of eight ions in two layers, with four indium and four selenium in each layer. The point group of bilayer InSe is C_{3v}, which

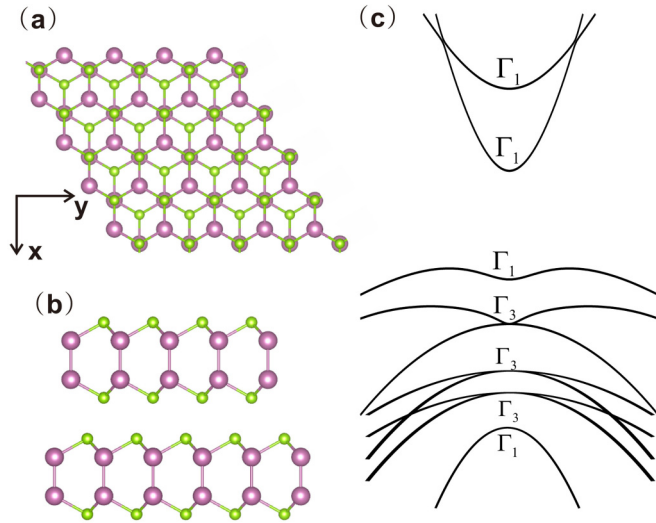*wenyang@csrc.ac.cn
†kchang@semi.ac.cn

FIG. 1. The crystal structure of AB-stacking bilayer InSe shown in (a) top view and (b) side view. (c) Sketch of the bilayer InSe electronic bands around the Γ point, omitting the spin-orbit coupling.

consists of six symmetry operations divided into three classes and hence three irreducible representations (see Table I). In the absence of SOC, we consider seven energy bands in the vicinity of the Fermi level, as shown in Fig. 1(c). Their orbital wave functions at the Γ point are (ordered with increasing energy) as follows:

TABLE I. Character table of group C_{3v} and the basis functions for each irreducible representation. Here (k_x, k_y, k_z) are the three Cartesian components of the momentum (which changes sign under spatial inversion) and (s_x, s_y, s_z) are the three Cartesian components of the spin (which remains invariant under spatial inversion).

C_{3v}	E	$2C_3$	σ_v	Basis functions
Γ_1	1	1	1	k_z
Γ_2	1	1	-1	s_z
Γ_3	2	-1	0	$(k_x, k_y)\ (s_x, s_y)$

$$|\Psi_{v_2}\rangle \sim k_z,$$
$$|\Psi_{v_5}\rangle \equiv (|\Psi_{v_5,x}\rangle, |\Psi_{v_5,y}\rangle) \sim (k_x,\ k_y) \text{ or } (s_x,\ s_y),$$
$$|\Psi_{v_4}\rangle \equiv (|\Psi_{v_4,x}\rangle, |\Psi_{v_4,y}\rangle) \sim (k_x,\ k_y) \text{ or } (s_x,\ s_y),$$
$$|\Psi_{v_3}\rangle \equiv (|\Psi_{v_3,x}\rangle, |\Psi_{v_3,y}\rangle) \sim (k_x,\ k_y) \text{ or } (s_x,\ s_y),$$
$$|\Psi_{v_1}\rangle \sim k_z,$$
$$|\Psi_{c_1}\rangle \sim k_z,$$
$$|\Psi_{c_2}\rangle \sim k_z,$$

where the symbol "$\sim$" tells us how these basis functions transform under C_{3v} operations; e.g., $|\Psi_{c_1}\rangle$, $|\Psi_{c_2}\rangle$, $|\Psi_{v_1}\rangle$, and $|\Psi_{v_2}\rangle$ remain invariant under all C_{3v} operations, and $|\Psi_{v_3}\rangle$, $|\Psi_{v_4}\rangle$, and $|\Psi_{v_5}\rangle$ transform like the two transverse components (x, y) or (s_x, s_y) of a vector.

In the basis $|\Psi_{v_5}\rangle$, $|\Psi_{v_4}\rangle$, $|\Psi_{v_3}\rangle$, $|\Psi_{v_2}\rangle$, $|\Psi_{v_1}\rangle$, $|\Psi_{c_1}\rangle$, $|\Psi_{c_2}\rangle$, the $\mathbf{k} \cdot \mathbf{p}$ Hamiltonian assumes the 7×7 block form:

$$\mathbf{H} = \begin{bmatrix} \mathbf{H}^{v_5,v_5} & \mathbf{H}^{v_5,v_4} & \mathbf{H}^{v_5,v_3} & \mathbf{H}^{v_5,v_2} & \mathbf{H}^{v_5,v_1} & \mathbf{H}^{v_5,c_1} & \mathbf{H}^{v_5,c_2} \\ \mathbf{H}^{v_4,v_5} & \mathbf{H}^{v_4,v_4} & \mathbf{H}^{v_4,v_3} & \mathbf{H}^{v_4,v_2} & \mathbf{H}^{v_4,v_1} & \mathbf{H}^{v_4,c_1} & \mathbf{H}^{v_4,c_2} \\ \mathbf{H}^{v_3,v_5} & \mathbf{H}^{v_3,v_4} & \mathbf{H}^{v_3,v_3} & \mathbf{H}^{v_3,v_2} & \mathbf{H}^{v_3,v_1} & \mathbf{H}^{v_3,c_1} & \mathbf{H}^{v_3,c_2} \\ \mathbf{H}^{v_2,v_5} & \mathbf{H}^{v_2,v_4} & \mathbf{H}^{v_2,v_3} & \mathbf{H}^{v_2,v_2} & \mathbf{H}^{v_2,v_1} & \mathbf{H}^{v_2,c_1} & \mathbf{H}^{v_2,c_2} \\ \mathbf{H}^{v_1,v_5} & \mathbf{H}^{v_1,v_4} & \mathbf{H}^{v_1,v_3} & \mathbf{H}^{v_1,v_2} & \mathbf{H}^{v_1,v_1} & \mathbf{H}^{v_1,c_1} & \mathbf{H}^{v_1,c_2} \\ \mathbf{H}^{c_1,v_5} & \mathbf{H}^{c_1,v_4} & \mathbf{H}^{c_1,v_3} & \mathbf{H}^{c_1,v_2} & \mathbf{H}^{c_1,v_1} & \mathbf{H}^{c_1,c_1} & \mathbf{H}^{c_1,c_2} \\ \mathbf{H}^{c_2,v_5} & \mathbf{H}^{c_2,v_4} & \mathbf{H}^{c_2,v_3} & \mathbf{H}^{c_2,v_2} & \mathbf{H}^{c_2,v_1} & \mathbf{H}^{c_2,c_1} & \mathbf{H}^{c_2,c_2} \end{bmatrix},$$

where $\mathbf{H}^{\mu\nu}$ is the block matrix between $|\Psi_\mu\rangle$ and $|\Psi_\nu\rangle$; e.g., $\mathbf{H}^{c_2,c_2}$ is a 1×1 block matrix associated with $|\Psi_{c_2}\rangle$, $\mathbf{H}^{v_4,v_4}$ is a 2×2 block matrix associated with $|\Psi^{v_4}\rangle$, and $\mathbf{H}^{c_2,v_4}$ is a 1×2 block matrix associated with the coupling between $|\Psi_{c_2}\rangle$ and $|\Psi_{v_4}\rangle$.

The theory of invariants provides a standard, systematic approach to constructing the $\mathbf{k} \cdot \mathbf{p}$ Hamiltonian based on the invariance of the crystal Hamiltonian $\hat{H}$ under all operations of the symmetry group C_{3v}. The invariance of the crystal Hamiltonian under an arbitrary symmetry operation $g \in C_{3v}$ shown in Table I dictates

$$\mathbf{D}^\alpha(g)\mathbf{H}^{\alpha\beta}(\hat{P}_g\mathcal{K}\hat{P}_g^{-1})\mathbf{D}^\beta(g^{-1}) = \mathbf{H}^{\alpha\beta}(\mathcal{K}), \qquad (1)$$

where $\mathbf{D}^\alpha(g)$ is the representation matrix of g in Γ_α and $\hat{P}_g\mathcal{K}\hat{P}_g^{-1}$ denotes the transformation of $\mathcal{K}$ (irreducible tensor components) under the operation g. In addition to the point group symmetry, the time-reversal symmetry imposes extra constraints on the $\mathbf{k} \cdot \mathbf{p}$ Hamiltonian. For bilayer InSe,

we can take all the basis functions shown in Fig. 1(c) to be real and hence invariant under time reversal, and then the time-reversal invariance of the crystal Hamiltonian $\hat{\theta}\hat{H}\hat{\theta}^{-1} = \hat{H}$ dictates the time-reversal invariance of the $\mathbf{k} \cdot \mathbf{p}$ Hamiltonian: $\hat{\theta}\mathbf{H}(\mathcal{K})\hat{\theta}^{-1} = \mathbf{H}(\mathcal{K})$, where $\hat{\theta}$ is the time-reversal operator.

In the absence of SOC and external fields, only the 2D momentum operator $\mathbf{k} \equiv (k_x, k_y)$ can appear in the $\mathbf{k} \cdot \mathbf{p}$ Hamiltonian of the bilayer InSe. Since $[k_x, k_y] = 0$, only three irreducible tensor operators can be constructed up to $O(k^2)$: $(k_x, k_y) \sim (x, y)$, $k_x^2 + k_y^2 \sim 1$, and $(k_y^2 - k_x^2, 2k_xk_y) \sim (x, y)$. Under time reversal, the first one is odd, while the latter two are even. By combining them with the symmetrized matrices in Table II, we can readily obtain all the invariants (shown in Table III) for each block of the $\mathbf{k} \cdot \mathbf{p}$ Hamiltonian. By using the invariants listed in Table III, we obtain the $\mathbf{k} \cdot \mathbf{p}$ Hamiltonian in Eq. (3):

$$\mathbf{H} = \text{diag}\{E_{v5}, E_{v5}, E_{v4}, E_{v4}, E_{v3}, E_{v3}, E_{v2}, E_{v1}, E_{c1}, E_{c2}\}$$
$$+ \mathbf{H}^{\text{off}}, \qquad (2)$$

where $E_{v5}, \ldots, E_{c2}$ are band-edge energies, and

$$
\mathbf{H}^{\text{off}} =
\begin{bmatrix}
C_{v5}k^2 + D_{v5}k_-^2 & -2D_{v5}k_xk_y & iB_{v5}^{v4}k_x & -iB_{v5}^{v4}k_y & iB_{v5}^{v3}k_x & -iB_{v5}^{v3}k_y & -iA_8k_y & -iA_9k_y & -iA_{10}k_y & -iA_{11}k_y \\
 & C_{v5}k^2 - D_{v5}k_-^2 & -iB_{v5}^{v4}k_y & -iB_{v5}^{v4}k_x & -iB_{v5}^{v3}k_y & -iB_{v5}^{v3}k_x & iA_8k_x & iA_9k_x & iA_{10}k_x & iA_{11}k_x \\
 & & C_{v4}k^2 + D_{v4}k_-^2 & -2D_{v4}k_xk_y & iBk_x & -iB_{v4}^{v3}k_y & -iAk_y & -iA_2k_y & -iA_3k_y & -iA_4k_y \\
 & & & C_{v4}k^2 - D_{v4}k_-^2 & -iB_{v4}^{v3}k_y & -iB_{v4}^{v3}k_x & iAk_x & iA_2k_x & iA_3k_x & iA_4k_x \\
 & & & & C_{v3}k^2 + D_{v3}k_-^2 & -2D_{v3}k_xk_y & -iA_1k_y & -iA_5k_y & -iA_6k_y & -iA_7k_y \\
 & & & & & C_{v3}k^2 - D_{v3}k_-^2 & iA_1k_x & iA_5k_x & iA_6k_x & iA_7k_x \\
 & & & & & & C_{v2}k^2 & A_{v2}^{v1}k^2 & A_{v2}^{c1}k^2 & A_{v2}^{c2}k^2 \\
 & & & & & & & C_{v1}k^2 & A_{v1}^{c1}k^2 & A_{v1}^{c2}k^2 \\
 & & & & & & & & C_1k^2 & A_{c1}^{c2}k^2 \\
 & & & & & & & & & C_2k^2
\end{bmatrix},
$$

$$(3)$$

where $k_-^2 = k_y^2 - k_x^2$. In the above we only keep the lowest-order contribution to each matrix element, and only give the matrix elements in the upper triangle since the $\mathbf{k} \cdot \mathbf{p}$ Hamiltonian is Hermitian. The parameters can be determined by comparing the energy band structure obtained from the $\mathbf{k} \cdot \mathbf{p}$ Hamiltonian to the first-principles calculations (see Appendix) in the vicinity of the Γ point [19,36–40]. The results are listed in Table IV. As shown in Fig. 2(a), our $\mathbf{k} \cdot \mathbf{p}$ model well reproduces the nonparabolic, Mexican hat dispersion—a unique feature of III-VI semiconductor few layers.

In the presence of SOC, the spin operator $\mathbf{s} = (s_x, s_y, s_z)$ can appear in the $\mathbf{k} \cdot \mathbf{p}$ Hamiltonian. Since $\mathbf{s}$ is an axial vector, we have $(s_x, s_y) \sim (R_x, R_y)$ and $s_z \sim R_z$ under C_{3v} operations. The nonzero invariants constructed from the electron spin operator alone are also listed in Table III. Here, we only display the lowest-order spin invariants; higher-order invariants could be obtained by multiplying the first-order invariants with C-G coefficients. With these invariants, we can construct the lowest-order SOC term $\mathbf{H}^{soc}$. By using the SOC-related invariants, we can construct the lowest-order spin-related term $\mathbf{H}^{soc}$ as given below:

$$
\begin{bmatrix}
0 & -i\lambda_{v5}s_z & 0 & 0 & 0 & 0 & 0 & i\lambda_{v5}^{v1}s_x & 0 & 0 \\
 & 0 & 0 & 0 & 0 & 0 & 0 & i\lambda_{v5}^{v1}s_y & 0 & 0 \\
 & & 0 & -i\lambda_{v4}s_z & 0 & 0 & 0 & i\lambda_{v4}^{v1}s_x & 0 & 0 \\
 & & & 0 & 0 & 0 & 0 & i\lambda_{v4}^{v1}s_y & 0 & 0 \\
 & & & & 0 & -i\lambda_{v3}s_z & 0 & i\lambda_{v3}^{v1}s_x & 0 & 0 \\
 & & & & & 0 & 0 & i\lambda_{v3}^{v1}s_y & 0 & 0 \\
 & & & & & & 0 & 0 & 0 & 0 \\
 & & & & & & & 0 & 0 & 0
\end{bmatrix},
$$

which contains 6 new parameters. The total Hamiltonian is $\mathbf{H}^{tot} = \mathbf{H} + \mathbf{H}^{soc}$. These new parameters are obtained by comparing the energy band structure obtained from $\mathbf{H}^{tot}$ to the first-principles calculations (including SOC) in the vicinity of the Γ point. The results are listed in Table IV.

As shown in Fig. 2(b), our $\mathbf{k} \cdot \mathbf{p}$ model captures two essential features of the InSe bilayer: the nonparabolic Mexican hat dispersion and the spin splitting due to the IRSOC. To make the IRSOC explicit, we can use the Lowdin perturbation theory to eliminate the valence band v_3 in favor of the topmost valence band v_1. This gives a second-order correction to the v_1 band: $\mathbf{H}_{\text{eff}}^{v_1,v_1} \propto \mathbf{H}^{v_1,v_3}\mathbf{H}^{v_3,v_1}$. For the C_{3v} symmetry group

of bilayer InSe, the Hamiltonian block $\mathbf{H}^{v_1,v_3} = (\mathbf{H}^{v_3,v_1})^\dagger = [iA_5k_y - i\lambda_{v_3}^{v_1}s_x, -iA_5k_x - i\lambda_{v_3}^{v_1}s_y]$ contains both (k_x, k_y) and (s_x, s_y) because they belong to the same irreducible representation Γ_3 (see Table I). As a result, their cross product in $\mathbf{H}_{\text{eff}}^{v_1,v_1}$ gives rise to the Rashba SOC term $\propto k_xs_y - k_ys_x$. By contrast, for the D_{3h} symmetry group of monolayer InSe, the mirror symmetry σ_h distinguishes (k_x, k_y) and (s_x, s_y) into different irreducible representations Γ_6 and Γ_5, so they cannot appear

TABLE II. Symmetrized matrices for bilayer InSe, where $\mathbb{I}_{2\times2}$ denotes the 2×2 identity matrix, τ_x, τ_y, τ_z are Pauli matrices acting on the orbital-band-edge Bloch states, $\Lambda_+ = [1, 0]$, and $\Lambda_- = [0, 1]$.

$\mathbf{H}^{\Gamma_1,\Gamma_1}$	$\Gamma_1 \otimes \Gamma_1^* = \Gamma_1$	$\Gamma_1 : 1$
$\mathbf{H}^{\Gamma_1,\Gamma_3}$	$\Gamma_1 \otimes \Gamma_3^* = \Gamma_3$	$\Gamma_3 : (\Lambda_-, -\Lambda_+)$
$\mathbf{H}^{\Gamma_3,\Gamma_3}$	$\Gamma_3 \otimes \Gamma_3^* = \Gamma_1 \oplus \Gamma_2 \oplus \Gamma_3$	$\Gamma_1 : \mathbb{I}_{2\times2}$
		$\Gamma_2 : \tau_y$
		$\Gamma_3 : (\tau_z, -\tau_x)$

TABLE III. Invariants for each block of the $\mathbf{k} \cdot \mathbf{p}$ Hamiltonian constructed from the 2D momentum operator up to the second order or from the spin operator. Here $k^2 \equiv k_x^2 + k_y^2$, τ_x, τ_y, τ_z are Pauli matrices acting on the orbital-band-edge Bloch states, and $\mathbf{H}_{1,1}$ stands for $\mathbf{H}_{1,1}^{\mu,\nu}$, $\{\mu, \nu\} = \{c_1, c_2, v_1, v_2\}$, $\mathbf{H}_{1,3}$ stands for $\mathbf{H}_{1,3}^{\mu,\nu}$, $\{\mu, \nu\} = \{v_3, v_4\}$, and $\mathbf{H}_{3,3}$ stands for $\mathbf{H}_{3,3}^{\mu,\nu}$, $\{\mu, \nu\} = \{v_3, v_4\}$. The imaginary factor i ensures that all the invariants remain invariant under time reversal.

$\mathbf{H}^{\Gamma_1,\Gamma_1}$	$\mathbf{H}^{\Gamma_3,\Gamma_3}$	$\mathbf{H}^{\Gamma_1,\Gamma_3}$
	$k^2\mathbb{I}_{2\times2}, s_z\tau_y$	$ik_x\Lambda_- - ik_y\Lambda_+$
k^2		
	$(k_y^2 - k_x^2)\tau_z - 2k_xk_y\tau_x$	$is_x\Lambda_+ + is_y\Lambda_-$

TABLE IV. Nonzero $\mathbf{k} \cdot \mathbf{p}$ parameters in the bilayer InSe $\mathbf{k} \cdot \mathbf{p}$ Hamiltonian.

Parameter	Value	Unit	Parameter	Value	Unit
E_{v5}	-1.369	eV	E_{v4}	-1.334	eV
E_{v3}	-1.272	eV	E_{v2}	-1.464	eV
E_{v1}	-0.6673	eV	E_{c1}	0.5378	eV
E_{c2}	1.23	eV	A	-0.0659	eV Å
A_1	-0.8798	eV Å	A_2	-2.29	eV Å
A_3	0.3483	eV Å	A_4	-4.9788	eV Å
A_5	0.1456	eV Å	A_6	-6.0990	eV Å
A_7	-0.0740	eV Å	A_8	1.5251	eV Å
A_9	0.1964	eV Å	A_{10}	4.0267	eV Å
A_{11}	0.1821	eV Å	C_2	0.4739	eV Å²
C_1	1.0827	eV Å²	C_{v1}	-1.3491	eV Å²
C_{v2}	-1.0686	eV Å²	C_{v3}	-2.9319	eV Å²
C_{v4}	-4.4253	eV Å²	C_{v5}	-4.2518	eV Å²
D_{v3}	0.2907	eV Å²	D_{v4}	-0.3833	eV Å²
D_{v5}	-0.4188	eV Å²	A_{v2}^{v1}	0.0618	eV Å²
A_{v2}^{c1}	-3.5983	eV Å²	A_{v2}^{c2}	0.0382	eV Å²
A_{v1}^{c1}	-0.1010	eV Å²	A_{v1}^{c2}	1.006	eV Å²
A_{c1}^{c2}	0.0267	eV Å²	B_{v5}^{v4}	0.102	eV Å
B_{v5}^{v3}	0.0151	eV Å	B_{v4}^{v3}	0.0739	eV Å
λ_{v3}	0.02	eV	λ_{v4}	0.08	eV
λ_{v5}	0.03	eV	λ_{v3}^{v1}	0.18	eV
λ_{v4}^{v1}	0.001	eV	λ_{v5}^{v1}	-0.06	eV

in the same Hamiltonian block and the Rashba SOC is absent. Also the Rashba SOC term $k_x s_y - k_y s_x$ cannot stay invariant under the σ_h operation. As shown in Fig. 1, the breaking mirror symmetry in bilayer InSe arises from its bilayer structure (see Fig. 1) and generates a built-in electric field (about 230 kV/cm) that can induce IRSOC. Finally, we notice that our model does not take into account the Dresselhaus SOC, which is a high-order term in $\mathbf{k}$. In principle, these high-order
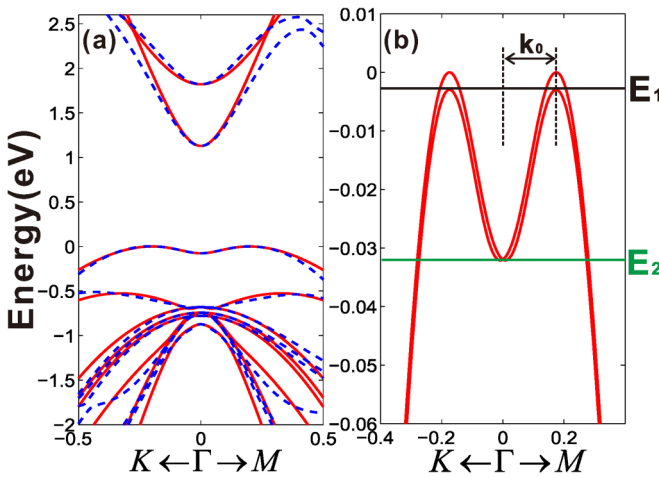

FIG. 2. (a) Energy band structure of bilayer InSe (without SOC) from our $\mathbf{k} \cdot \mathbf{p}$ model Hamiltonian (red solid lines) and first-principles calculations (blue dashed lines). (b) Detailed structure of the topmost valence band (including SOC) from our $\mathbf{k} \cdot \mathbf{p}$ model; $\mathbf{k_0} = 0.175/$Å is the wave vector of valence band maxima.

terms can be included using the invariant theory, but this would make the multiband $\mathbf{k} \cdot \mathbf{p}$ model very complicated, so we choose to neglect these terms in the $\mathbf{k} \cdot \mathbf{p}$ model, but include these effects in Sec. III by using the tight-binding model.

III. SPIN-CHARGE CONDUCTIVITY

According to the Onsager relation, the spin-to-charge conductivity is equal to the charge-to-spin conductivity [23,41]. And the conductivity reads

$$\sigma_{\alpha\beta}^{SGE} = -\frac{e}{2\pi} \int \frac{d^2p}{(2\pi)^2} \text{Tr}[J_\alpha G^R(\mu) s_\beta G^A(\mu)], \quad (4)$$

where $J_\alpha = e v_\alpha = e \partial \mathbf{H}^{tot}/\partial k_\alpha$ ($\alpha = x, y$) is the current operator, s_β is the spin operator, and $G^{R(A)}$ is the retarded (advanced) Green's function corresponding to the unperturbed Hamiltonian $\mathbf{H}^{tot}$, taken at the chemical potential μ. For a clean-limit situation, the S-C conductivity $\sigma_{\alpha\beta}^{SGE}$ shown in Eq. (4) becomes infinite.

A. Clean-limit Drude coefficient

In the limit of a clear system, the carrier lifetime $\tau \to \infty$ and the conductivity $\sigma_{\alpha\beta}^{SGE}$ diverges as $\sigma_{\alpha\beta}^{SGE} = \mathbf{D}_{\alpha\beta}^{SGE} \tau$, where

$$\mathbf{D}_{\alpha\beta}^{SGE} = -\text{Re} \int \frac{d^2\mathbf{k}}{2\pi} [f(E_{-\mathbf{k}}) - f(E_{+\mathbf{k}})]$$

$$\times \frac{\langle -, \mathbf{k}|s_\alpha|+, \mathbf{k}\rangle \langle +, \mathbf{k}|J_\beta|-, \mathbf{k}\rangle}{E_{-,\mathbf{k}} - E_{+,\mathbf{k}} + i0^+} \quad (5)$$

is the Drude coefficient for spin-charge conversion [28], with $f(E) = 1/(e^{(E-\mu)/(k_B T)} + 1)$ the Fermi distribution, $E_{+\mathbf{k}}$ ($E_{-\mathbf{k}}$) the upper (lower) spin-split branch of the topmost valence band, and $|\pm, \mathbf{k}\rangle$ the corresponding wave functions. Here the chemical potential μ can be tuned by gate voltages [29]. Due to the rotational invariance of our $\mathbf{k} \cdot \mathbf{p}$ Hamiltonian $\mathbf{H}^{tot}$ around the z axis, only $\mathbf{D}_{xy}^{SGE}$ and $\mathbf{D}_{yx}^{SGE}$ are nonzero and they obey $\mathbf{D}_{xy}^{SGE} = -\mathbf{D}_{yx}^{SGE}$. At zero temperature, the integral over the $\mathbf{k}$ space in Eq. (5) is limited to a small region in which $E_{-\mathbf{k}} < \mu < E_{+\mathbf{k}}$; i.e., the lower spin-split branch is occupied, $f(E_{-\mathbf{k}}) = 1$, and the upper spin-split branch is empty, $f(E_{+\mathbf{k}}) = 0$. As shown in Fig. 3(a), the zero-temperature clean-limit spin-charge response as a function of μ exhibits a giant peak at the first intraband Lifshitz transition point E_1 [as indicated by the black line in Fig. 2(b)] and exhibits a sudden decrease at the second intraband Lifshitz transition point E_2 [as indicated by the green line in Fig. 2(b)].

The variation of $\mathbf{D}_{xy}^{SGE}$ with the chemical potential μ near the valence band maxima ($\mu > E_1$) can be analytically obtained. As shown in Fig. 3(b), when μ slightly intersects the topmost valence band, the upper spin-split branch of this valence band gives rise to two concentric Fermi circles (blue lines). According to Eq. (5), contribution to $\mathbf{D}_{xy}^{SGE}$ comes from the integral of $\mathbf{k}$ over the region obeying $E_{-\mathbf{k}} < \mu < E_{+\mathbf{k}}$ [shaded region in Fig. 3(b)]. The radius of the outer (inner) circle is $k_0 + k_F$ ($k_0 - k_F$), where k_0 is the radius of the Mexican hat indicated in Fig. 2(a) and Fig. 3(b), and $k_F \equiv \sqrt{2m^*|\mu|}$ is the Fermi momentum relative to the valence band maxima, with m^* the effective mass of valence band maxima.
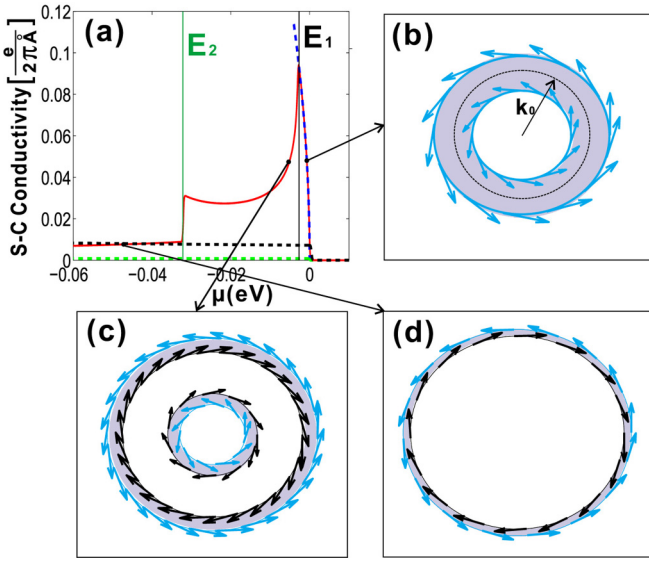
FIG. 3. (a) Spin-charge response $\mathbf{D}_{xy}^{SGE}$ calculated by using multi-band $\mathbf{k} \cdot \mathbf{p}$ model (red solid line) and analytic equation (blue dashed line) vs chemical potential μ for clean-limit ($\tau \to \infty$) InSe bilayer. The black and green dashed lines are the spin-charge response for clean-limit two-dimensional electron gas formed at oxide interface (LaAlO$_3$/SrTiO$_3$) and (n-InSb/In$_x$Al$_{1-x}$Sb) quantum well. (b)–(d) show the spin texture (arrows) on the Fermi circles at different chemical potentials: blue (black) lines for the upper (lower) spin-split branch of the topmost valence band. Black dashed line in Fig. 2(b) indicate the valence band maxima energy Fermi circles (radius of Mexican hat).

Numerical results show that in the circular region shown in Fig. 3(b), $E_{+,\mathbf{k}} - E_{-,\mathbf{k}}$ is almost a constant (denoted by ΔE). For relatively small k, we can approximately describe the spin texture of $|\pm, \mathbf{k}\rangle$ by an effective RSOC term $\alpha_{\text{eff}}(k_x s_y - k_y s_x)$, which gives $|\pm, \mathbf{k}\rangle = (1/\sqrt{2})[1, \pm i e^{i\phi}]$, and the spin-dependent part of v_y as $v_y = -\alpha_{\text{eff}} s_x$, with ϕ the azimuth angle of $\mathbf{k}$. Then we can use $\langle -, \mathbf{k} | s_x | +, \mathbf{k} \rangle = -i \cos \phi$ and $\langle -, \mathbf{k} | v_y | +, \mathbf{k} \rangle = -i \alpha_{\text{eff}} \cos \phi$ to obtain

$$\mathbf{D}_{xy}^{SGE} \approx -\frac{e \alpha_{\text{eff}}}{4\pi \Delta E} A = -\frac{e \alpha_{\text{eff}}}{\Delta E} k_0 k_F, \quad (6)$$

where $A = 4\pi k_0 k_F$ is the area of the circular region shown in Fig. 3(b). By fitting the energy band structure shown in Fig. 2(b), we obtain $\Delta E = 3$ meV, $k_0 = 0.175/\text{Å}$, and $m^* = 1.418 m_e$ (m_e is the free-electron mass). By fitting Eq. (6) to the numerically calculated clean-limit spin-charge response, we obtain $\alpha_{\text{eff}} = -8$ meV Å, so that

$$\mathbf{D}_{xy}^{SGE} = \frac{e}{2\pi} \frac{1.8}{\text{Å}\sqrt{\text{eV}}} \sqrt{|\mu|}.$$

As shown in Fig. 3(a), this fitting formula (blue dashed line) agrees well with the exact numerical results from the multiband $\mathbf{k} \cdot \mathbf{p}$ model (red solid line) when $\mu > E_1$. At the Lifshitz transition point E_1, the Drude coefficient peak of bilayer InSe (red solid line) is one order of magnitude larger than that of the LaAlO$_3$/SrTiO$_3$ oxide interface (black dashed line). According to Eq. (6), this strong enhancement arises from the large area of the circular region in Fig. 3(b), i.e., the Mexican hat dispersion of the topmost valence band.
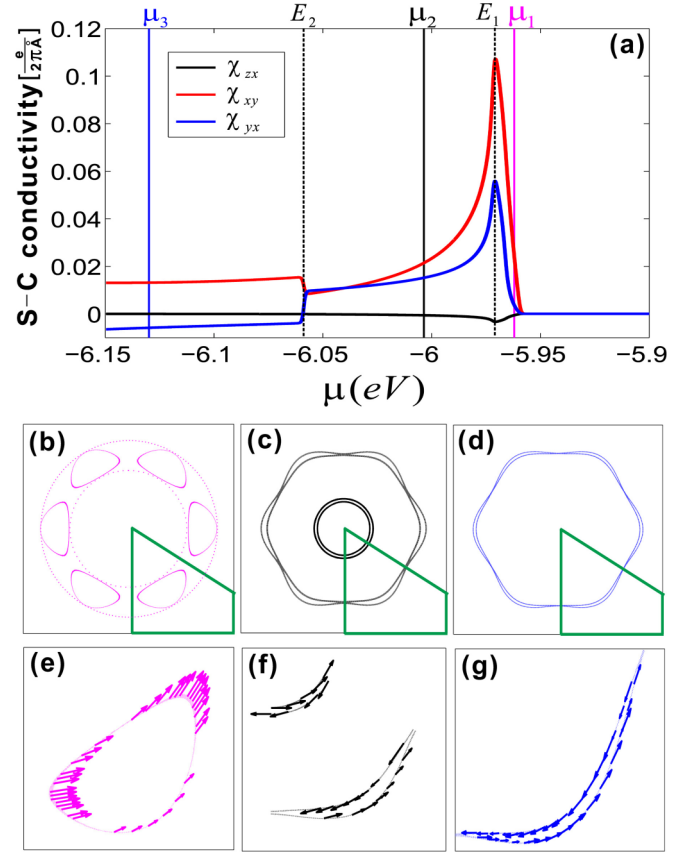

FIG. 4. (a) Spin-charge conductivities $\mathbf{D}_{xy}^{SGE}$ (red), $\mathbf{D}_{yx}^{SGE}$ (blue), and $\mathbf{D}_{zx}^{SGE}$ (black) from the tight-binding model at $T = 5$ K. (b)–(d) show the Fermi contours corresponding to chemical potential μ_1, μ_2, and μ_3 indicated in panel (a). (e)–(g) show the in-plane spin texture of the Fermi contour in the green box of (b)–(d).

When μ drops below the first intraband Lifshitz transition point $E_1 (E_2 < \mu < E_1)$, the lower spin-split branch begins to contribute and gives two concentric circles (black lines) with the same, clockwise spin orientation (black arrows), as shown in Fig. 3(c). In this case, a contribution to $\mathbf{D}_{xy}^{SGE}$ comes from the integral of $\mathbf{k}$ over the shaded region in Fig. 3(c), which decreases with increasing $|\mu|$. Moreover, the upper spin-split branch and the lower spin-split branch have opposite spin orientations; their contributions to $\mathbf{D}_{xy}^{SGE}$ tend to cancel each other. These considerations explain the sharp decrease of $\mathbf{D}_{xy}^{SGE}$ after μ drops below E_1. When μ goes further below the second intraband Lifshitz transition point $E_2 (\mu < E_2)$, there are only two Fermi circles with opposite spin orientations as shown in Fig. 3(d), and $\mathbf{D}_{xy}^{SGE}$ remains nearly constant, similar to the case of conventional 2DEGs with Rashba SOC.

Next, we confirm the results above by utilizing the tight-binding model, which includes anisotropic effects neglected in our $\mathbf{k} \cdot \mathbf{p}$ model, such as the Dresselhaus SOC. In Fig. 4(a), the two intraband Lifshitz transitions E_1 and E_2, the sharp peak of the Drude coefficient at E_1, and its abrupt change at E_2 can be readily identified, similarly to Fig. 3(a). The Fermi contours shown in Figs. 4(b)– 4(d) and the spin textures shown in Figs. 4(e)–4(g) are also qualitatively similar to those in Figs. 3(b)– 3(d), respectively. For example, in Fig. 4(b), the spin orientations on the inner dashed circle and the outer
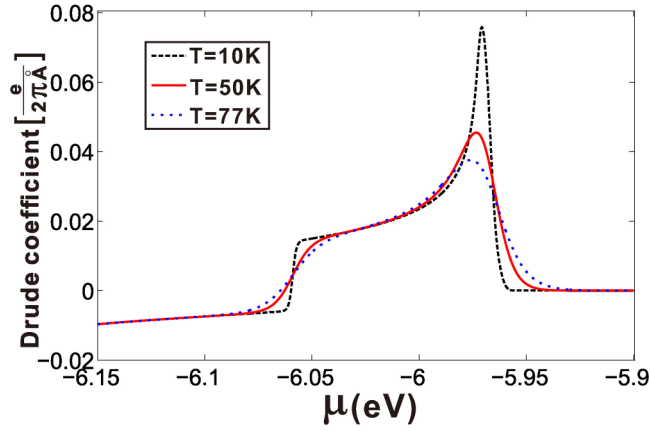
FIG. 5. S-C conductivity $\mathbf{D}_{yx}^{SGE}$ at different temperatures: $T = 10$ K (black line), 50 K (red line), 77 K (blue line).

FIG. 6. (a) Density of states near the valence band maxima of InSe bilayer. (b) S-C conductivity σ_{xy}^{SGE} vs chemical potential μ for InSe bilayer (solid line), oxide interface LaAlO$_3$/SrTiO$_3$ (dashed line), and quantum well n-InSb/In$_x$Al$_{1-x}$Sb (dotted line) for different disorder strengths $n_i v_0^2 = 0.4 \times 10^{-3}$ (eV Å)^2 (red lines), $n_i v_0^2 = 0.8 \times 10^{-3}$ (eV Å)^2 (blue lines), and $n_i v_0^2 = 1.2 \times 10^{-3}$ (eV Å)^2 (green lines).

dashed circle are both counterclockwise, consistent with the results shown in Fig. 3(b). The difference is that the tight-binding model includes high-order anisotropic effects, which breaks the relation $\mathbf{D}_{xy}^{SGE} = -\mathbf{D}_{yx}^{SGE}$, and the corresponding Dresselhaus SOC effect allows a small out-of-plane Drude coefficient $\mathbf{D}_{zx}^{SGE}$ [black line in Fig. 4(a)]. The Fermi circles in Figs. 3(b)– 3(d) also becomes Fermi contours in Figs. 4(b)– 4(d). However, differently from the isotropic situation shown in Figs. 3(b)– 3(d), the Fermi contours and the spin textures in Figs. 4(b)–4(g) obtained by using the tight-binding model indicate a C_6 symmetry. The C_6 symmetry for in-plane spin texture stems from the combination of the time-reversal symmetry and the C_{3v} symmetry of bilayer InSe (see Appendix).

Finally, we consider the influence of temperature on the clean-limit response. As shown in Fig. 5, increasing the temperature generally tends to smooth out the peak of the Drude coefficient. However, the peak still has good visibility even in the liquid-nitrogen temperature.

B. Disorder effects

In this section, we study the disorder effects on S-C conductivity. For a disordered system, $G^{R(A)}$ in Eq. (4) should be understood as disorder-averaged Green's functions:

$$G^{R(A)} = \frac{1}{\mu - \mathbf{H}^{tot} \pm i\Gamma}, \quad (7)$$

where $\Gamma = \hbar/(2\tau)$ is the level broadening due to the disorder. For randomly distributed short-range impurities described by a random potential $V(r)$ with Gaussian correlation $\langle V(r)V(r') \rangle = n_i v_0^2 \delta(r - r')$, we can use the Born approximation to obtain $\Gamma = n_i v_0^2 N(\mu)$ [23], where n_i is the impurity density, v_0 is the disorder scattering potential, and $N(\mu)$ is the density of states (DOS) at the chemical potential μ. As shown in Fig. 6(a), the DOS (and hence the level broadening Γ) shows a sharp peak at the first Lifshitz transition point E_1 (indicated by the black line), and then decrease continuously as the chemical potential μ goes deeper into the valence band.

By using Eq. (4), we calculate the zero-temperature S-C conductivity vs chemical potential μ for different disorder strengths and plot the results in Fig. 6(b). Here, the S-C conductivity is calculated within the Born approximation
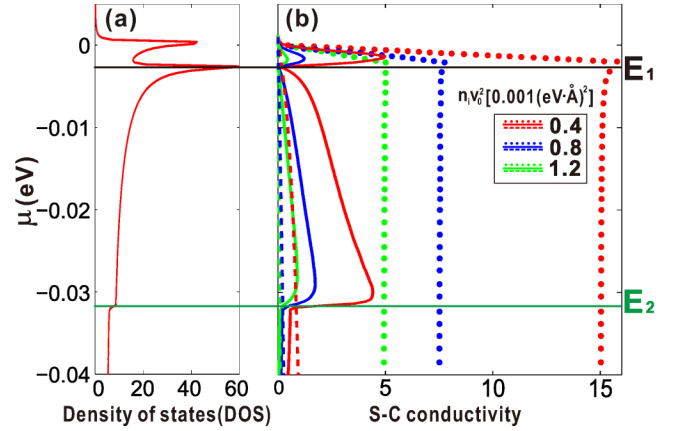
without using a vertex correction [27]. Compared with the Drude coefficient shown in Fig. 3(a), the S-C conductivity shown in Fig. 6(b) exhibits two important differences. First, the large level broadening Γ at E_1 suppresses the peak at E_1 [see Fig. 3(a)] and shifts this peak to a slightly higher chemical potential [see Fig. 6(b)]. Second, when the chemical potential μ drops below E_1 and goes deeper into the valence band ($E_2 < \mu < E_1$), the rapid decrease of the level broadening Γ overcompensates the decrease of the Drude coefficient, so that the S-C conductivity increases with decreasing μ, as opposed to the Drude coefficient in Fig. 3(a). When the disorder strength $n_i v_0^2$ increases, the level broadening also increases, so the S-C conductivity decreases monotonically. Importantly, for the same disorder strength, the S-C conductivity in the InSe bilayer [solid line in Fig. 6(b)] is nearly five times that of the oxide interface LaAlO$_3$/SrTiO$_3$ [dashed line in Fig. 6(b)]. Compared with InSe bilayer, the small DOS of quantum well n-InSb/In$_x$Al$_{1-x}$Sb leads to a much longer lifetime τ, making the S-C conductivity larger than that in bilayer InSe under the same disorder strength.

IV. CONCLUSION

We have adopted the standard invariant theory to derive a 20-band $\mathbf{k} \cdot \mathbf{p}$ Hamiltonian for the electronic structure of bilayer InSe. This $\mathbf{k} \cdot \mathbf{p}$ model shows that an *intrinsic* Rashba spin-orbit coupling (IRSOC) in InSe without any external electric fields is generated by the mirror symmetry breaking of the bilayer. Interestingly, the interplay between the IRSOC and unique Mexican hat dispersion at the topmost of the valence band give rise to a big spin-charge conductivity. We have confirmed these findings by using the first-principles calculations and tight-binding model. Since light doping usually implies a long carrier lifetime, this makes it possible to observe experimentally the intraband Lifshitz transitions and the resulting peak in the spin-charge conductivity. Since the Rashba SOC and the Mexican hat dispersion also exist in other

bilayer III-VI semiconductors, we expect similar phenomena in these systems. These findings may pave the way for the application of bilayer III-VI semiconductors in 2D spintronic devices.

APPENDIX

1. Detailed information on the first-principles calculations

To obtain the bilayer InSe band structure, we use the Vienna *ab initio* simulation package (VASP) [42] within the local density approximation (LDA) [43] and the projector augmented wave (PAW) [44] pseudopotential. We set the kinetic energy cutoff to 600 eV for the wave function expansion and the k-point grid is sampled by sums over $12 \times 12 \times 1$. The electronic self-consistent calculations converge up to a precision of 10^{-8} eV in total energy difference. A slab model, together with a vacuum layer larger than 20 Å, is employed. The calculated lattice parameters of the bilayer InSe are $a = 3.953$Å, $d_{InIn} = 2.741$ Å, and $d_{SeSe} = 5.298$ Å. Interlayer distance parameter $d = 8.32$ Å. Our numerical results shown in Fig. 2 (blue dashed lines), with an energy vertical gap at the Γ point of 1.205 eV, are in good agreement with the previous works [15,45].

There are many different minimization methods that can be used. Here, we perform the least-squares fitting [46] within the range $k < 0.15/$Å without taking SOC into consideration, and the results are shown in Fig. 2(a). Since the spin-charge conductivity we calculated near the topmost valence band is induced by Rashba spin-orbit coupling, we fit out the spin-dependent terms by comparing the spin-splitting energy calculated by the **k** · **p** model including SOC with the splitting energy obtained from first-principles calculation along the $\Gamma \rightarrow M$ direction.

2. Tight-binding calculations

For bilayer InSe, the tight-binding Hamiltonian with SOC taken into account has been developed in this Appendix. In 2016, a 32×32 atomic orbital basis tight-binding Hamiltonian $\mathbf{H}_{TB}$ was constructed [15], and the band structure calculated by this model without SOC taken into consideration is shown in Fig. 7(a). We can expand this tight-binding Hamiltonian into a 64×64 atomic orbital space with spin. The new Hamiltonian can be developed as $\mathbf{H}_{TB}^{ASO} = \mathbf{H}_{TB} + \mathbf{H}^{ASO}$, where $\mathbf{H}^{ASO}$ stands for the SOC Hamiltonian that stems from on-site atomic spin-orbit coupling.
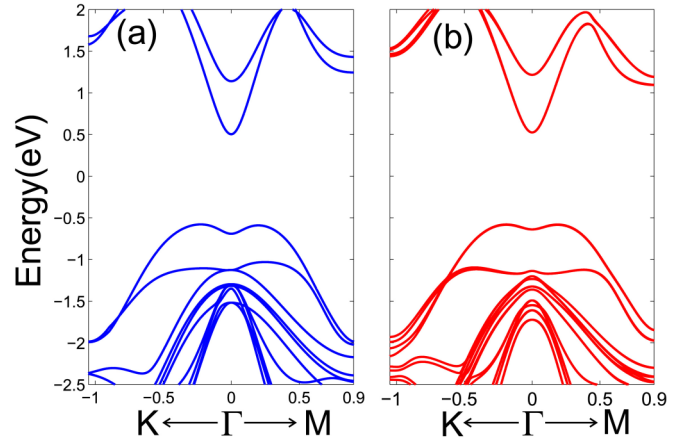

FIG. 7. (a) Band structure calculated by tight-binding model without SOC taken into consideration. (b) Band structure calculated by density functional theory including SOC.

Generally speaking, the SOC appears as an additional term in the Schrödinger equation given by

$$\hat{H}_{SO} = \frac{1}{2m^2c^2}(\vec{\nabla}V \times \vec{p}) \cdot \vec{S}, \quad (A1)$$

where m stands for free-electron mass, c is the light speed, $\vec{p}$ is canonical momentum, and $\vec{S} = \hbar/2\vec{s}$ is the spin vector operator. The potential gradient $\vec{\nabla}V$ can be seen as an electric field. Under atomic orbital representation, this SOC operator can be rewritten as a term that couples the spin and angular momentum as

$$\hat{H}_{SO} = \xi_\alpha \vec{L} \cdot \vec{S} = \xi_\alpha(L_x S_x + L_y S_y + L_z S_z), \quad (A2)$$

where ξ_α is the parameter determined by the atomic radial wave function. We only take the sp orbital into account in our atomic tight-binding Hamiltonian; therefore parameters ξ_α depend only on atoms $\xi_{\mathbf{In}}$, $\xi_{\mathbf{Se}}$. Since the SOC has its largest effect on electrons at the nucleus, the hopping matrix elements of the SOC Hamiltonian between different atoms are assumed to be zero. Therefore, the SOC Hamiltonian under atomic orbit representation has a diagonal block format.

In the atomic basis $\{1s^{M_1}, 1p_x^{M_1}, 1p_y^{M_1}, 1p_z^{M_1}, 1s^{M_2}, 1p_x^{M_2}, 1p_y^{M_2}, 1p_z^{M_2}, 1s^{X_1}, 1p_x^{X_1}, 1p_y^{X_1}, 1p_z^{X_1}, 1s^{X_2}, 1p_x^{X_2}, 1p_y^{X_2}, 1p_z^{X_2}, 2s^{M_1}, 2p_x^{M_1}, 2p_y^{M_1}, 2p_z^{M_1}, 2s^{M_2}, 2p_x^{M_2}, 2p_y^{M_2}, 2p_z^{M_2}, 2s^{X_1}, 2p_x^{X_1}, 2p_y^{X_1}, 2p_z^{X_1}, 2s^{X_2}, 2p_x^{X_2}, 2p_y^{X_2}, 2p_z^{X_2}\}$, where the upper indexes $M_{1/2}$ and $X_{1/2}$ stand for indium and selenium atoms located in the first/second sublayer, front index 1 or 2 represents which layer the atom is located in, and we can easily write

$$\mathbf{H}^{ASO} = \begin{bmatrix} 1 & 0 \\ 0 & 1 \end{bmatrix} \otimes \begin{bmatrix} \xi_{\mathbf{In}}H_{SO} & 0 \\ 0 & \xi_{\mathbf{Se}}H_{SO} \end{bmatrix},$$

$$H_{SO} = \begin{bmatrix} 1 & 0 \\ 0 & 1 \end{bmatrix} \otimes \begin{bmatrix} 0 & 0 & 0 & 0 \\ 0 & 0 & -is_z & is_y \\ 0 & is_z & 0 & -is_x \\ 0 & -is_y & is_x & 0 \end{bmatrix}, \quad (A3)$$

where s_x, s_y, s_z are the Pauli matrix. The direct production in $\mathbf{H}^{ASO}$ expands the monolayer SOC Hamiltonian into the

bilayer SOC Hamiltonian. In our calculation we fit the topmost valence band spin splitting obtained by using the tight-binding model with the first-principles calculation results and finally get $\xi_{In} = 0.01$ eV, $\xi_{Se} = 0.02$ eV. Under the tight-binding model with these two atomic SOC parameters, we can obtain a spin-split band structure, and its topmost valence band agrees well with the band structure calculated by density functional theory shown in Fig. 7(b).

By using this tight-binding Hamiltonian, we step forward and obtain the results shown in Fig. 4. As we can see, in Figs. 4(b)–4(g) in-plane spin texture indicates a C_6 symmetry that is not contained in a C_{3v} group. To understand this, we can define a state $\psi_1(k, \alpha, \theta)$ located at definite energy μ, where α is the angle between the wave vector $\vec{k}$ and the x axis, and the angle between the spin and x axis is θ. In the C_{3v} lattice, the crystal symmetry operation C_3 ensures that there are two other states $\psi_2(k, \alpha + 2\pi/3, \theta + 2\pi/3)$ and $\psi_3(k, \alpha - 2\pi/3, \theta - 2\pi/3)$ also at constant energy surface μ. In conclusion, a simple equation can be

obtained:

$$
\begin{aligned}
E[\psi_1(k, \alpha, \theta)] &= E[\psi_2(k, \alpha + 2\pi/3, \theta + 2\pi/3)] \\
&= E[\psi_3(k, \alpha - 2\pi/3, \theta - 2\pi/3)] = \mu.
\end{aligned}
\tag{A4}
$$

Besides crystal symmetry, the time-reversal symmetry establishes a new relationship:

$$
\begin{aligned}
E[\psi_4(k, \alpha + \pi, \theta + \pi)] &= E[\psi_5(k, \alpha + 5\pi/3, \theta + 5\pi/3)] \\
&= E[\psi_6(k, \alpha - \pi/3, \theta - \pi/3)] \\
&= \mu.
\end{aligned}
\tag{A5}
$$

Hence, for a definite state $\psi(k, \alpha, \theta)$ at constant energy surface μ, five other states are created by the C_6 operation still at energy μ. This proves that the in-plane spin texture at the constant energy surface shown in Fig. 4 satisfies C_6 symmetry, which was developed by the combination of C_3 symmetry and time-reversal invariance.

[1] R. W. Damon and R. W. Redington, Phys. Rev. **96**, 1498 (1954).

[2] P. K. Larsen, S. Chiang, and N. V. Smith, Phys. Rev. B **15**, 3200 (1977).

[3] C. De Blasi, G. Micocci, A. Rizzo, and A. Tepore, Phys. Rev. B **27**, 2429 (1983).

[4] A. Khater, M. Balkanski, C. Julien, and M. Weber, Phys. Rev. B **37**, 8278 (1988).

[5] A. Segura, B. Mari, J. Martinez-Pastor, and A. Chevy, Phys. Rev. B **43**, 4953 (1991).

[6] P. Gomes da Costa, M. Balkanski, and R. F. Wallis, Phys. Rev. B **43**, 7066 (1991).

[7] P. Gomes da Costa, R. G. Dandrea, R. F. Wallis, and M. Balkanski, Phys. Rev. B **48**, 14135 (1993).

[8] M. O. D. Camara, A. Mauger, and I. Devos, Phys. Rev. B **65**, 125206 (2002).

[9] F. J. Manjón, A. Segura, V. Muñoz-Sanjosé, G. Tobías, P. Ordejón, and E. Canadell, Phys. Rev. B **70**, 125201 (2004).

[10] D. Errandonea, A. Segura, F. J. Manjón, A. Chevy, E. Machado, G. Tobias, P. Ordejón, and E. Canadell, Phys. Rev. B **71**, 125206 (2005).

[11] D. Errandonea, D. Martínez-García, A. Segura, J. Haines, E. Machado-Charry, E. Canadell, J. C. Chervin, and A. Chevy, Phys. Rev. B **77**, 045208 (2008).

[12] V. Zólyomi, N. D. Drummond, and V. I. Fal'ko, Phys. Rev. B **87**, 195403 (2013).

[13] D. V. Rybkovskiy, A. V. Osadchy, and E. D. Obraztsova, Phys. Rev. B **90**, 235302 (2014).

[14] P. Li and I. Appelbaum, Phys. Rev. B **92**, 195129 (2015).

[15] S. J. Magorrian, V. Zólyomi, and V. I. Fal'ko, Phys. Rev. B **94**, 245431 (2016).

[16] T. Cao, Z. Li, and S. G. Louie, Phys. Rev. Lett. **114**, 236602 (2015).

[17] S. Lei, L. Ge, Z. Liu, S. Najmaei, G. Shi, G. You, J. Lou, R. Vajtai, and P. M. Ajayan, Nano. Lett. **13**, 2777 (2013).

[18] D. A. Bandurin, A. V. Tyurnina, G. L. Yu, A. Mishchenko, V. Zolyomi, S. V. Morozov, R. K. Kumar, R. V. Gorbachev, Z. R. Kudrynskyi, S. Pezzini, Z. D. Kovalyuk, U. Zeitler, K. S. Novoselov, A. Patane, L. Eaves, I. V. Grigorieva, V. I. Fal'ko, A. K. Geim, and Y. Cao, Nat. Nanotechnol. **12**, 223 (2017).

[19] M. Zhou, R. Zhang, J. Sun, W.-K. Lou, D. Zhang, W. Yang, and K. Chang, Phys. Rev. B **96**, 155430 (2017).

[20] S. J. Magorrian, V. Zólyomi, and V. I. Fal'ko, Phys. Rev. B **96**, 195428 (2017).

[21] H. F. Xu, W. Wang, Y. F. Zhao, X. Q. Zhang, Y. Feng, J. Tu, C. Y. Gu, Y. Z. Sun, C. Liu, Y. F. Nie, I. C. E. Turcu, Y. B. Xu, and L. He, AIP Adv. **8**, 055123 (2018).

[22] S. Nagel, A. Baldereschi, and K. Maschke, J. Phys. C **12**, 1625 (1979).

[23] V. M. Edelstein, Solid State Commun. **73**, 233 (1990).

[24] A. Johansson, J. Henk, and I. Mertig, Phys. Rev. B **93**, 195440 (2016).

[25] R. L. Kallaher, J. J. Heremans, N. Goel, S. J. Chung, and M. B. Santos, Phys. Rev. B **81**, 075303 (2010).

[26] S. D. Ganichev, P. Schneider, V. V. Bel'kov, E. L. Ivchenko, S. A. Tarasenko, W. Wegscheider, D. Weiss, D. Schuh, B. N. Murdin, P. J. Phillips, C. R. Pidgeon, D. G. Clarke, M. Merrick, P. Murzyn, E. V. Beregulin, and W. Prettl, Phys. Rev. B **68**, 081302(R) (2003).

[27] A. Dyrdał and J. Barnaś, Phys. Rev. B **92**, 165404 (2015).

[28] G. Seibold, S. Caprara, M. Grilli, and R. Raimondi, Phys. Rev. Lett. **119**, 256801 (2017).

[29] E. Lesne, Y. Fu, S. Oyarzun, J. C. Rojas-Sánchez, D. C. Vaz, H. Naganuma, G. Sicoli, J.-P. Attané, M. Jamet, E. Jacquet, J.-M. George, A. Barthélémy, H. Jaffrès, A. Fert, M. Bibes, and L. Vila, Nat. Mater. **15**, 1261 (2016).

[30] C. Huang, M. Milletarì, and M. A. Cazalilla, Phys. Rev. B **96**, 205305 (2017).

[31] I. Garate and M. Franz, Phys. Rev. Lett. **104**, 146802 (2010).

[32] H. J. Zhang, S. Yamamoto, B. Gu, H. Li, M. Maekawa, Y. Fukaya, and A. Kawasuso, Phys. Rev. Lett. **114**, 166602 (2015).

[33] D. S. Smirnov and L. E. Golub, Phys. Rev. Lett. **118**, 116801 (2017).

[34] M. Offidani, M. Milletarì, R. Raimondi, and A. Ferreira, Phys. Rev. Lett. **119**, 196801 (2017).

[35] D. Xiao, G.-B. Liu, W. Feng, X. Xu, and W. Yao, Phys. Rev. Lett. **108**, 196802 (2012).

[36] P. Pfeffer and W. Zawadzki, Phys. Rev. B **53**, 12813 (1996).

[37] S. L. Chuang and C. S. Chang, Phys. Rev. B **54**, 2491 (1996).

[38] K. Kim, W. R. L. Lambrecht, B. Segall, and M. van Schilfgaarde, Phys. Rev. B **56**, 7363 (1997).

[39] D. J. Dugdale, S. Brand, and R. A. Abram, Phys. Rev. B **61**, 12933 (2000).

[40] P. E. Faria Junior, T. Campos, C. M. O. Bastos, M. Gmitra, J. Fabian, and G. M. Sipahi, Phys. Rev. B **93**, 235204 (2016).

[41] K. Shen, G. Vignale, and R. Raimondi, Phys. Rev. Lett. **112**, 096601 (2014).

[42] G. Kresse and J. Furthmüller, Phys. Rev. B **54**, 11169 (1996).

[43] W. Kohn and L. J. Sham, Phys. Rev. **140**, A1133 (1965).

[44] P. E. Blöchl, Phys. Rev. B **50**, 17953 (1994).

[45] X. Yang, B. Sa, H. Zhan, and Z. Sun, J. Mater. Chem. C **5**, 12228 (2017).

[46] C. M. O. Bastos, F. P. Sabino, P. E. F. Junior, T. Campos, J. L. F. D. Silva, and G. M. Sipahi, Semicond. Sci. Technol. **31**, 105002 (2016).